Rare Metal Materials and Engineering
Volume ***, Issue ***, *****
Available online at **www.rmme.ac.cn**

Science Press

Cite this article as: Rare Metal Materials and Engineering

ARTICLE

DOI: https://doi.org/10.12442/j.issn.1002-185X.20260201

Dual-phase multi-principal element alloy with synergistic diffusion barrier for p-type skutterudite thermoelectric interfaces

Fandong Zhang[1†], Binhao liu[1†], Jingwen Huang[1], Cong Qiu[1], Jian Chen[1], and Jialun Zhang[1,2,*]

[1]National Key Laboratory of Power Semiconductor and Integration Technology, Engineering Research Center of Advanced Semiconductor Technology and Application of Ministry of Education, College of Semiconductors (College of Integrated Circuits), Hunan University, Changsha 410082, China

[2]Changsha Semiconductor Technology and Application Innovation Research Institute, Changsha 410082, China

Abstract: The inferior thermal stability of p-type skutterudites and their electrical contacts has severely limited the reliability of skutterudite-based thermoelectric devices. In this work, a dual-phase multi-principal element alloy interlayer, $CoFeNiMo_{0.75}$, is engineered via adequate Mo alloying to establish a multiple diffusion barrier effect while maintaining thermal expansion matching. Mo dissolved in the FCC matrix intensifies lattice distortion to hinder elemental diffusion, while the dispersed dendritic Mo-rich μ-phase precipitates exhibit weak reactivity and increase the effective diffusion-path tortuosity. Owing to this dual-phase synergistic mechanism, the $CoFeNiMo_{0.75}/La_{0.8}Ti_{0.1}Ga_{0.1}Fe_{3.3}Co_{0.7}Sb_{12}$ interface demonstrates exceptional thermal stability. After aging at 823 K for 600 h, the interfacial contact resistivity increased only from ~2.51 $\mu\Omega\cdot cm^2$ to ~3.22 $\mu\Omega\cdot cm^2$, following parabolic kinetics with an ultralow rate constant of ~0.028 $\mu\Omega\cdot cm^2\cdot h^{-1/2}$, while the shear strength remained largely stable at ~16 MPa. These results showcase the potential of the dual-phase strategy in achieving robust, multi-level diffusion barriers for next-generation thermoelectric interfaces.

Key words: p-type skutterudite; multi-principal element alloys; dual-phase structure; diffusion barrier; thermoelectric interfaces

1 Introduction

Thermoelectric (TE) devices have attracted significant attention for solid-state heat-to-electricity conversion in applications such as waste-heat recovery, deep-space power supply, and deep-sea exploration[1-4]. In conventional TE device design, the interface is usually guided by several well-established criteria: (i) matching the coefficient of thermal expansion (CTE) to reduce thermal stress, (ii) matching work functions to minimize electrical barriers, and (iii) suppressing elemental diffusion to delay reaction-layer growth[5,6]. However, for practical TE devices, the service lifespan is governed by the coupled reliability of the n-type and p-type thermoelectric materials and their interfaces[7-9]. Therefore, to achieve high stability, interface design must transcend simple joining and adopt a comprehensive material-interface integrated regulation approach.

This is particularly critical for skutterudite-based (SKD-based) thermoelectric modules. Skutterudite are the most promising candidates for medium-temperature power generation owing to their favorable electrical transport properties, intrinsically low lattice thermal conductivity, and good thermal stability[10-12]. However, the degradation or interfacial failure of either the n- or p-type leg will inevitably

Received date:
Foundation item: Key Research and Development Program of Department of Science and Technology of Hunan Province (Grant No. 2024JK2102), the Fundamental Research Funds for the Central Universities (Grant No. 531118010967), and the "111 Center" (Project No. B25033).
Corresponding author: Jialun Zhang, Ph.D., Assistant professor, National Key Laboratory of Power Semiconductor and Integration Technology, Engineering Research Center of Advanced Semiconductor Technology and Application of Ministry of Education, College of Semiconductors (College of Integrated Circuits), Hunan University, Changsha 410082, China, Changsha Semiconductor Technology and Application Innovation Research Institute, Changsha 410082, China, Tel: 13677370799, E-mail: zhangjialun@hnu.edu.cn

compromise the reliability of the entire device. This issue is more pronounced in p-type $CoSb_3$-based skutterudites (P-SKD), where Fe substitution at Co sites is commonly used to introduce hole carriers, but it can also cause charge imbalance and reduce the phase stability [13-15]. Once integrated into a module, this P-SKD instability accelerates interfacial reactions, increases contact resistance, and deteriorates joint strength[16-20]. To address this issue, various interlayer materials, ranging from pure metals to binary and ternary alloys (e.g., Nb[21], Ti[22], Ti-Al[23-25], Ti-Ni[26], Ni-Cr[27], Fe-V[28], Ti-Al-Si[26], Ti-Nb-Co[29], Fe-Cr-Co[30], Fe-Cr-Mo[31]), have been investigated. Nevertheless, most studies have focused on suppressing interfacial reactions from the interlayer side, while few have attempted to mitigate the inherent skutterudite decomposition itself by inhibiting elemental diffusion out of the P-SKD.

To overcome this limitation, the multi-principal element alloys (MPEAs) offer a promising platform for interlayer design due to their broad compositional space, tunable phase constitution, lattice-distortion effect, and intrinsic sluggish diffusion effects[32]. Recently, MPEAs have emerged as highly promising diffusion barrier layers for skutterudite joints, demonstrating exceptional diffusion-blocking capabilities[33]. Furthermore, their phase constitution can be deliberately adjusted beyond those available in conventional single-phase alloys[34-37]. More importantly, research indicates that the physical properties of MPEAs can undergo profound modifications when evolving into a dual-phase structure[38]. In structural materials, dual-phase MPEAs have already demonstrated exceptional mechanical advantages, often overcoming the conventional strength-ductility trade-off through the synergistic interaction between matrix and secondary phases[39-41]. This suggests that a dual-phase structure may also produce remarkable benefits in diffusion blocking. This architecture could not only leverages lattice distortion of the matrix, but also introduces phase boundaries and precipitate networks that collectively act as potential barriers to reshape diffusion pathways. Therefore, the dual-phase MPEA provide a powerful opportunity to design interlayers in which thermal expansion compatibility and diffusion blocking are achieved simultaneously.

In this work, a Mo-alloyed CoFeNi-based dual-phase MPEA interlayer, $CoFeNiMo_{0.75}$, was engineered to substantially suppress elemental interdiffusion while matching the coefficient of thermal expansion with both parent materials. Initial joints between p-type skutterudite ($La_{0.8}Ti_{0.1}Ga_{0.1}Fe_{3.3}Co_{0.7}Sb_{12}$) and Cu-W pseudo-alloy electrodes were fabricated using this dual-phase MPEA interlayer via diffusion bonding and then subjected to thermal aging at 823 K for various durations to assess thermal stability. By integrating atom-scale microstructure analysis with reaction-diffusion theory, the interfacial reaction products were identified, and the interfacial evolution behavior was quantified. Owing to a synergistic multiple blocking effect arising from the lattice-distorted matrix phase and the chemically stable dendritic Mo-rich precipitate phase, the CoFeNiMo$_{0.75}$/$La_{0.8}Ti_{0.1}Ga_{0.1}Fe_{3.3}Co_{0.7}Sb_{12}$ interface exhibits an exceptional thermal stability: the contact resistivity increased with an ultralow parabolic rate constant of approximately 0.028 $\mu\Omega\cdot cm^2\cdot h^{-1/2}$ while the shear strength remained at ~16 MPa after 600 h of aging. These findings provide a multiple diffusion barrier strategy based on the dual-phase synergistic effect in MPEAs, advancing the reliable operation of skutterudite-based thermoelectric devices.

2 Experiment Section

2.1 Materials synthesis and joints preparation

The thermoelectric materials with nominal compositions of p-type skutterudite $La_{0.8}Ti_{0.1}Ga_{0.1}Fe_{3.3}Co_{0.7}Sb_{12}$ (abbreviated as P-SKD) were synthesized through a melting-annealing method combined with spark plasma sintering (SPS). High-purity raw materials, including Ga ingot (99.999%, Alfa Aesar), La pieces (99.9%, Alfa Aesar), Ti granules (99.99%, Alfa Aesar), Co pieces (99.9%, Alfa Aesar), Fe granules (99.98%, Alfa Aesar), and Sb shot (99.999%, Alfa Aesar), were weighed according to the chemical compositions, respectively. The weighed raw materials were loaded into a carbon crucible, sealed in a quartz tube under high vacuum (<10^{-4} Pa). The tubes were slowly heated to 1423 K and maintained for 5 h, then rapidly quenched in room-temperature water. The quenched samples were annealed at 973 K for 150 h, and subsequently ground into powder with a particle size of less than 50 μm, and finally densified using spark plasma sintering system (LABOX-650F, SINTER LAND) under a pressure of 60 MPa at 873 K for 10 min.

The Mo-MPEA with nominal composition of $CoFeNiMo_{0.75}$ was synthesized through an induction melting method. The Mo-MPEA was fabricated into 200 μm-thick disks. They were first connected to Cu-W pseudo-alloy (CuW, nominal composition (*wt.*%): Cu40W60) electrodes, and then further connected to skutterudites via SPS. Specifically, an Fe layer was electroplated on the surface of the Cu-W prior to connection with Mo-MPEA.

2.2 Microstructure characterization

Phase identification was performed by X-ray diffraction analysis (XRD) (Bruker D8 ADVANCE) with Cu Kα radiation (λ = 1.5406 Å). The microstructure and chemical compositions were characterized by field emission scanning electron microscopy (SEM) (MIRA4 LMH, TESCAN) coupled with energy-dispersive X-ray spectroscopy (EDS) (NordlysMax2, Oxford) and electron backscattered diffraction (EBSD). Nanoscale microstructure analysis was performed using transmission electron microscopy (TEM) (Talos F200i, FEI) equipped with an EDS detector (6T-100RT, Bruker). The phase distributions and crystallographic features were identified using high-angle annular dark-field (HAADF) and se-

lected-area electron diffraction (SAED). The TEM samples were prepared by focused ion beam (FIB) (Helios 5 CX, Thermo Scientific) milling.

2.3 Physical Property Measurements

The CTE was characterized using a dilatometer (DIL 402 Expedis Classic, NETZSCH). Tensile tests were conducted using a Kammrath-Weiss micro-tensile stage with a nominal strain rate of 1×10^{-4} s^{-1}. Digital image correlation (DIC) strain-field analysis was employed to characterize the precise strain, utilizing a 2-D optical measurement system and evaluated by the VIC-2D system. In-situ nanoindentation mapping was performed using a high-precision nanomechanical testing system (FT-NMT04, Oxford Instruments). The tested region was carefully polished to achieve a surface roughness below 10 nm. The mapping was conducted over a 100 μm × 100 μm area with a step size of 1 μm. Based on these measurements, spatial distribution maps of indentation hardness (H_{IT}) and reduced modulus (E_r) were obtained. The contact resistivity (ρ_c) was quantified at 300 K using a custom-built apparatus by the four-probe method.

3 Results and discussion

3.1 Dual-phase multi-principal element alloy interlayer

Motivated by previous high-throughput screening results indicating that Mo has a weaker reaction with SKD[7], Mo was alloyed into the CoFeNi-based system, thereby markedly modifying its phase constitution[41]. The $CoFeNiMo_{0.75}$ composition was selected to construct a dual-phase Mo-MPEA barrier layer while maintaining acceptable CTE compatibility with P-SKD. Based on a mixture rule[42], the theoretical CTE of $CoFeNiMo_{0.75}$ at 273K is approximately 9.71×10^{-6} K^{-1}, corresponding to a CTE mismatch of about 10% with P-SKD.

As shown in Figure 1(a), Figure 2 and Table 1, the ternary CoFeNi alloy exhibits a single-phase FCC structure, whereas $CoFeNiMo_{0.75}$ presents additional weak diffraction peaks besides the dominant FCC phase. The magnified pattern in the 2θ range of 41°-45° further confirms the presence of weak diffraction signals from the Mo-rich μ phase with a hexagonal structure, which can be indexed as Co_7Mo_6[43]. Specifically, the calculated VEC of $CoFeNiMo_{0.75}$ is approximately 8.40, supporting FCC matrix retention, whereas the atomic size and electronegativity mismatch introduced by Mo and the Mo-rich TCP phase regions in the Fe-Mo and Co-Mo systems account for the precipitation of Mo-rich μ phases. In addition, XRD refinement shows that the FCC lattice parameter increases from 3.586 Å for CoFeNi to 3.600 Å for $CoFeNiMo_{0.75}$. This result indicates that part of the Mo atoms is dissolved into the FCC matrix, inducing lattice expansion and local lattice distortion. Therefore, Mo addition partially dissolves into the FCC lattice to form a solid solution, while the excess Mo promotes the precipitation of a Mo-rich secondary phase, ultimately forming a dual-phase MPEA.

Table 1. Parameters of melting point, electronegativity, valence electron concentration (VEC), and atomic radius for Fe, Co, Ni, and Mo[44,45].

Elements	Melting point (℃)	Electronegativity	VEC	Atomic radius (Å)
Fe	1538	1.83	8	1.2412
Co	1495	1.88	9	1.251
Ni	1455	1.91	10	1.2459
Mo	2623	2.16	6	1.3626

To evaluate how this dual-phase Mo-MPEA affects macroscopic performance, its tensile behavior and thermal expansion compatibility were first investigated. As shown in Figure 1(b), CoFeNi exhibits relatively low yield strength but high tensile ductility, which is typical of FCC solid-solution alloys. In contrast, $CoFeNiMo_{0.75}$ shows a much higher yield strength and tensile strength, but its elongation is substantially reduced. This can be attributed to the combined effects of solid solution strengthening from Mo atoms in the FCC matrix and second-phase reinforcement from the hard μ phase. In addition to mechanical strength, thermal expansion compatibility is a critical requirement for a reliable skutterudite joint. As shown in Figure 1(c), the CoFeNi alloy already exhibits good thermal expansion compatibility with P-SKD. After alloying with the low-CTE refractory element Mo, the alloy evolves into a dual-phase structure. Nevertheless, its CTE remains well matched with that of P-SKD over the investigated temperature range (as further shown by the temperature-dependent CTE curves in the inset). This preserved CTE compatibility is beneficial for mitigating thermal-mismatch-induced residual stress during cooling and long-term aging, thereby supporting the use of Mo-MPEA as a diffusion barrier layer for P-SKD joints.

To further reveal the crystallographic and strain characteristics of the Mo-MPEA, BSE and nanoindentation analysis were investigated. Figure 1(d) reveals a heterogeneous morphology consisting of a continuous matrix phase and dispersed dendritic secondary phases. The inset in (d) shows a magnified

BSE image of a selected region, where the nanoindentation array can be clearly observed with an interval of 1 μm between adjacent indentation points. Correspondingly, as shown in Figure 1(e, f), the μ phase displays a higher reduced modulus (E_r) and nanoindentation hardness (H_{IT}) than the FCC matrix, explicitly confirming that the Mo-rich secondary phase acts as a mechanically reinforced region responsible for the macroscopic strength improvement observed in Figure 1(b).

As further detailed by the EBSD analysis in Figure 1(g, h), the μ phase is distributed as a discontinuous network along the dendrite boundaries of the continuous FCC matrix. The IPF map shows different crystallographic orientations within the FCC matrix, indicating a polycrystalline dendritic structure rather than a single-orientation solidification morphology. The phase map confirms that the μ phase is mainly confined to the dendritic regions, consistent with Mo segregation and subsequent μ phase formation during solidification. Moreover, the KAM map in Figure 1(i) shows that the majority of the grain interiors exhibit low KAM values (blue regions, <1°), suggesting a relatively low dislocation density in these zones. Conversely, significant strain localization is observed at the grain boundaries and phase interfaces, characterized by elevated KAM values. Such a microstructure may simultaneously contribute to mechanical strengthening through solid-solution strengthening and secondary phase reinforcement, and to diffusion blocking by Mo alloying enhances lattice distortion and increasing the tortuosity of elemental transport pathways during interfacial reactions. It is worth noting that the coherent or semi-coherent boundaries between the FCC matrix and μ phases may also induce dense localized strain fields, which can potentially serve as energetic barriers to trap and impede migrating atoms [39,40]. Building on the microstructure and crystallographic characteristics of the Mo-MPEA, the subsequent investigation systematically analyzes the interfacial microstructure evolution during thermal aging to further evaluate its long-term service reliability.

3.2 Interfacial microstructure evolution during thermal aging

Electrical interface between P-SKD thermoelectric materials and Cu-W pseudo-alloy electrodes were fabricated by solid-state diffusion bonding using Mo-MPEA as the interlayer. As shown in Figure 3(a), the Mo-MPEA enables effective bonding between the P-SKD, and the electrode. A dense and defect-free interface with metallurgical bonding characteristics was obtained. In addition, to improve the overall bonding process and quality between the Cu-W electrode and the Mo-MPEA, an approximately 2 μm-thick Fe layer was electroplated onto the surface of the Cu-W electrode before bonding (Figure 3(b)). The excellent metallurgical compatibility between the Fe layer and the Mo-MPEA stabilizes the overall bonding, while its limited mutual solubility with the Cu-W electrode prevents excessive reactions, which enhance the overall thermal stability of the joint.

Figure 3(c-g) summarizes the microstructural evolution of the Mo-MPEA/P-SKD interface during thermal aging at 823K and establishes a quantitative description of the reaction-layer growth. In the as-bonded state, a thin reaction layer with a thickness of approximately 4.2 μm is already formed at the Mo-MPEA/P-SKD interface. After aging for 48 h and 120 h, the reaction layer thickens to approximately 10.4 μm and 13.9 μm, respectively. Further aging to 360 h and 600 h increases the reaction layer thickness to approximately 21.2 μm and 26.1 μm, respectively. Although the reaction layer grows continuously with aging time, it remains compact and well bonded to both the Mo-MPEA interlayer and the P-SKD. No severe interfacial cracking is detected, suggesting that the interfacial reaction proceeds in a controlled manner rather than causing rapid structural degradation. Notably, as highlighted by the yellow dotted boxes in Figure 3(f, g), the μ phase effectively pins the reaction interface and thins the reaction layer on the Mo-MPEA side, thereby disrupting the continuity of the reaction front and forcing it to grow through a spatially confined, uneven, and interpenetrating pathway rather than by rapid planar advance.

The line-scan result in Figure 3(h) further confirms the development of a chemically graded reaction zone after 600 h aging. From the Mo-MPEA side, Fe, Co, Ni, and Mo participate in the interfacial reaction, while Sb-, Ga-, La-, and Ti-containing species originate from the P-SKD side. Sb is enriched within the reaction layer, indicating that Sb diffusion remains the dominant process governing interfacial reaction layer growth. However, the line-scan exhibits relatively sharp transitions at both sides of the reaction zone, suggesting that long-range elemental interdiffusion is effectively restricted. In particular, the limited diffusion of Sb and Ga into the Mo-MPEA side demonstrates the diffusion blocking ability of the interlayer.

Therefore, the interfacial evolution behaviors, combined with the crystallographic and microstructural characteristics previously detailed in Figure 1, collectively elucidate the diffusion-blocking mechanisms. The Mo-MPEA with exceptional diffusion-blocking capabilities can be attributed to the combined effects: (i) the partial dissolution of Mo into the FCC matrix intensifies lattice distortion, which enhances the sluggish diffusion effect; (ii) due to limited solubility in the FCC matrix, Mo drives the precipitation of Mo-rich topologically close-packed μ phases. Characterized by high melting points and robust chemical stability, these precipitates exhibit minimal reactivity with the p-type skutterudite; (iii) distributed throughout the matrix, the dendritic Mo-rich μ precipitates act as physical barriers that force migrating elements to deviate from direct routes, thereby significantly increasing the diffusion-path tortuosity. It should be noted that although incorporating Mo significantly enhances the diffusion-blocking capa-

bility of the MPEA interlayer, its content was not further increased. Excessive Mo addition would further decrease the CTE of the interlayer, thereby enlarging the thermal expansion mismatch with P-SKD and elevating the risk of interfacial failure induced by thermomechanical mismatch[46,47].

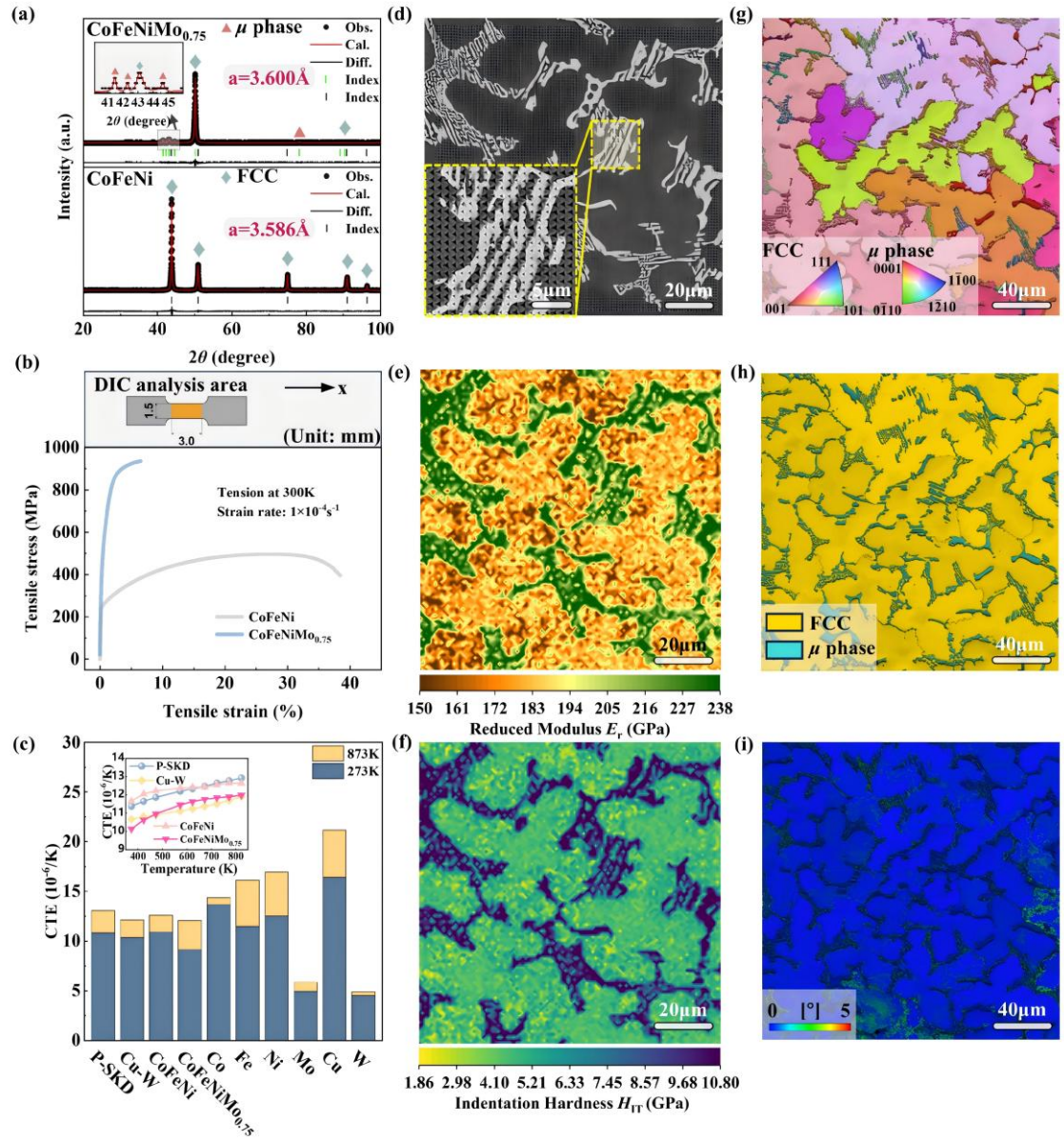

Figure 1. Microstructure, mechanical response, and thermal expansion behavior of the Mo-alloyed CoFeNi-based dual-phase multi-principal element alloy (Mo-MPEA) interlayer. (a) X-ray diffraction (XRD) patterns of CoFeNi and $CoFeNiMo_{0.75}$, showing the formation of a dual-phase structure after Mo alloying. The inset in (a) presents a magnified view of the 2θ range from 41° to 45°. (b) Room-temperature tensile stress-strain curves of CoFeNi and $CoFeNiMo_{0.75}$ at a strain rate of 1×10^{-4} s^{-1}. The inset in (b) shows the geometry of the tensile specimen, where the yellow-marked region denotes the area selected for digital image correlation (DIC) analysis. (c) Comparison of the coefficients of thermal expansion (CTEs) of P-SKD, Cu-W, CoFeNi, $CoFeNiMo_{0.75}$, and typical metal materials. The inset in (c) shows the temperature-dependent CTE curves of P-SKD, Cu-W, CoFeNi, and $CoFeNiMo_{0.75}$ in the range of 375-875 K. (d) Backscattered electron (BSE) images of the Mo-MPEA, showing the typical dendritic morphology with the secondary phase distributed in the dendritic regions. The inset in (d) shows a magnified BSE image of the selected region, where the nanoindentation array can be clearly observed with an interval of 1 μm between adjacent indentation points. (e, f) Nanoindentation mapping of reduced modulus (E_r) and indentation hardness (H_{IT}), showing the mechanical heterogeneity associated with the dual-phase architecture. (g) Inverse pole figure (IPF) orientation map (h) phase map and (i) kernel average misorientation (KAM) map of the Mo-MPEA.

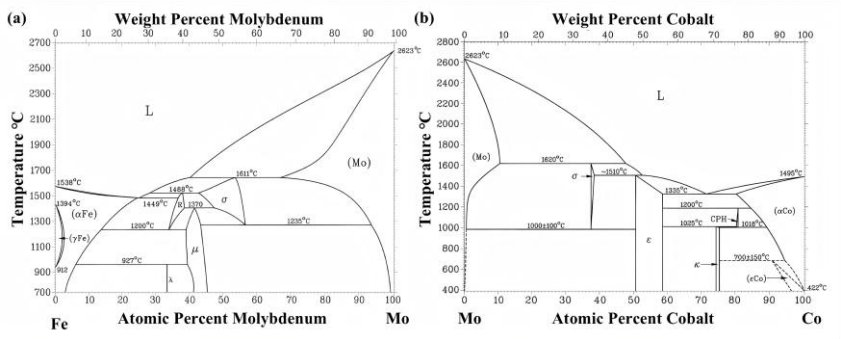

Figure 2. Binary phase diagrams of (a) Fe-Mo and (b) Co-Mo systems, showing the phase equilibria and TCP phase regions associated with Mo-containing transition-metal alloys.

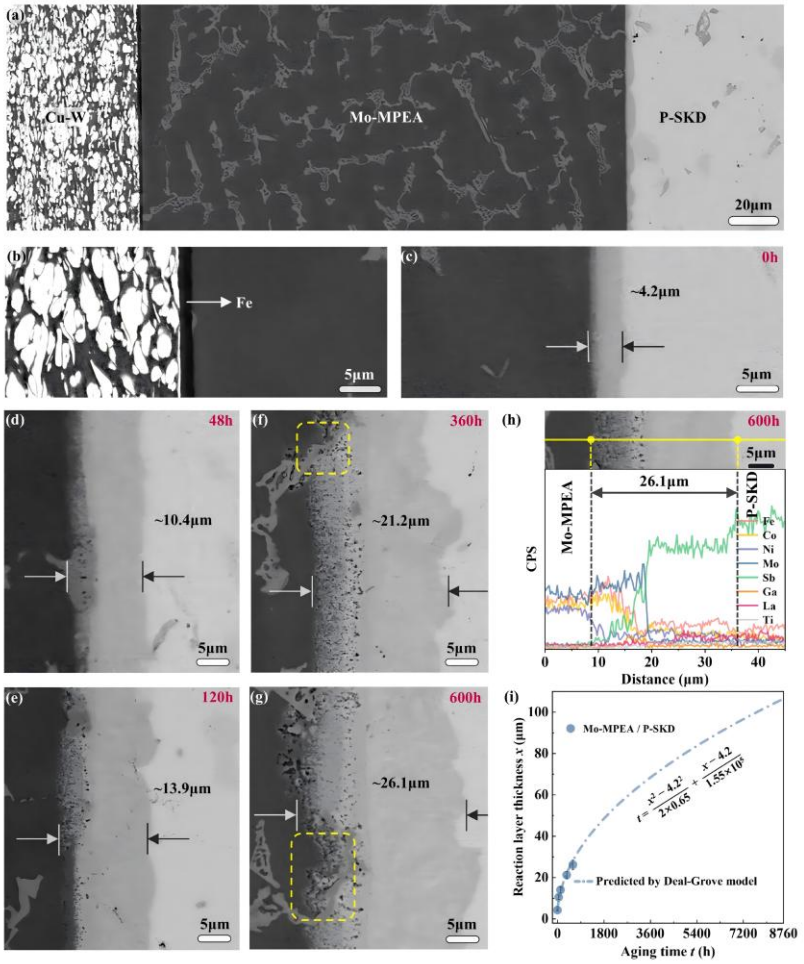

Figure 3. Interfacial evolution throughout thermal aging at 823 K for durations of 0, 48, 120, 360, and 600 h. (a) BSE image of the Cu-W/Fe/Mo-MPEA/P-SKD interface for 0h. (b) BSE image of the Cu-W/Fe/Mo-MPEA interface for 0h. (c-g) BSE images of the Mo-MPEA/P-SKD interface after aging for 0, 48, 120, and 360 h, 600h respectively, showing the gradual thickening of the interfacial reaction layer without severe cracking. (h) BSE image and corresponding scanning electron microscopy (SEM) - energy-dispersive X-ray spectroscopy (EDS) elemental line scans of the interface after aging for 600 h. (i) Experimental and predicted reaction-layer thickness as a function of aging time, fitted using a Deal-Grove model.

Based on the thermal aging test results, the growth kinetics of the reaction layer were quantified using the Deal-Grove model, as shown in Figure 3(i). The experimentally measured thicknesses agree well with the fitted curve, indicating that the reaction-layer growth is predictable. Benefiting from the ro-

bust barriers discussed above, the extrapolated thickness at one year remains below approximately 110 μm, indicating that the reaction layer grows progressively instead of undergoing uncontrolled thickening.

3.3 Interfacial reaction mechanism

To further clarify the microstructural evolution of the Mo-MPEA/P-SKD interface, the interfacial reactions between these two materials were systematically analyzed. Figure 4(a) reveals the interfacial structure between the Mo-MPEA and the P-SKD. The total thickness of the reaction layer is approximately 4.2 μm, and the yellow solid line marks the original contact interface. The SAED patterns taken from regions A-C confirm that the Mo-MPEA phase is retained near the interlayer side. Specifically, regions A and B correspond to the original Mo-MPEA matrix, whereas region C still exhibits the characteristic diffraction features of Mo-MPEA but contains dissolved Ga and Sb (Figure 4(b)), indicating the formation of a Ga/Sb-containing Mo-MPEA solid solution, denoted as (Mo-MPEA, Ga/Sb)$_{ss}$. Whereas region D is indexed as cubic $GaMo_3$. Regions E and F correspond to hexagonal (Co, Fe, Ni)Sb, region G is identified as orthorhombic $LaSb_2$, and region H retains the cubic P-SKD structure.

Based on the high-angle annular dark-field (HAADF) scanning transmission electron microscopy (STEM) image and the corresponding STEM-EDS elemental maps shown in Figure 4(b), Co, Fe, and Ni are identified as the main diffusing elements from the Mo-MPEA side, and their diffusion extent follows the order of Ni > Co > Fe. This difference suggests that Ni is the most mobile transition-metal species in the present reaction system, whereas Fe shows the most limited diffusion From the P-SKD side, Sb and Ga are the dominant diffusing elements. However, their diffusion into the Mo-MPEA is strongly confined. In particular, the Mo-MPEA shows an effective blocking ability against Sb, despite its relatively high diffusivity. Sb is restricted to a narrow region of approximately 1 μm near the interface. Ga is also localized mainly within the reaction layer, where it participates in the formation of $GaMo_3$. The elemental interdiffusion induces partial decomposition of the P-SKD. Subsequently, metallic elements from the Mo-MPEA can participate in the interfacial reaction, resulting in the formation of interpenetrating network reaction structure consisting mainly of (Co, Fe, Ni)Sb and $LaSb_2$. This process can be schematically expressed as:

$$La_x(Co, Fe)_4Sb_{12} \rightarrow (Co, Fe)Sb_3 + (Co, Fe)Sb_2 + LaSb_2 \quad (1)$$

$$(Co, Fe, Ni) + (Co, Fe)Sb_2 \rightarrow (Co, Fe, Ni)Sb \quad (2)$$

The interfacial bonding mechanism between the Mo-MPEA and the P-SKD can therefore be summarized as follows: (i) Sb, Ga, Ni, Co, and Fe are the principal elements involved in interfacial interdiffusion; (ii) this interdiffusion destabilizes the skutterudite structure and promotes the formation of hexagonal (Co, Fe, Ni)Sb and orthorhombic $LaSb_2$; (iii) the interdiffusion process disrupts the entropy-stabilized state of the multi-principal element alloy near the interface, giving rise to competitive growth between the (Co, Fe, Ni)Sb phase and the $GaMo_3$ phase. As a result, an interpenetrating network reaction structure is formed at the interface. Accordingly, the interfacial microstructure can be described as: Cu-W /Fe/ Mo-MPEA / (Mo-MPEA, Ga/Sb)$_{ss}$ / $GaMo_3$ + (Co, Fe, Ni) Sb/ (Co, Fe, Ni) Sb + $LaSb_2$ / P-SKD.

3.4 Thermal stability of interfacial properties

Figure 5 evaluates the property stability of the Mo-MPEA/P-SKD joint by combining electrical contact measurements with mechanical shear testing. Figure 5(a) shows the microprobe-based electrical testing system used for contact-resistivity measurements. To verify the reliability of the method, Figure 5(b) compares the measured R×A values as a function of probe spacing for several reference materials. The linear dependence of R×A on distance, together with the close agreement between the measured and reference resistivities of Cu, Constantan, Invar, and SKD, confirms that the measurement configuration is sufficiently reliable for evaluating the interfacial contact resistance. As shown in Figure 5(c), the contact resistivity of the Mo-MPEA/P-SKD joint increases only gradually during aging. The value rises from approximately 2.51 μΩ·cm^2 in the initial state to about 3.22 μΩ·cm^2 after 600 h. The absence of an abrupt increase indicates that the interface does not suffer from rapid electrical degradation. Instead, the moderate increase in contact resistivity is consistent with the progressive thickening of the interfacial reaction layer observed in Figure 3.

Figure 5(d) further correlate the electrical response with aging kinetics. The contact resistivity follows the empirical relation indicating an approximately linear dependence on $t^{1/2}$. This behavior is consistent with the diffusion-controlled reaction-layer growth established in Figure 3. The extrapolated contact resistivity at 8760 h remains below approximately 5.1 μΩ·cm^2, supporting the long-term electrical stability of the joint. The inset in Figure 5(d) illustrates the contact resistance sample during the testing process. The evolution of contact resistivity (ρ_c) as a function of the square root of aging time ($t^{1/2}$) is presented in Figure 5(e). As summarized in Table 2, the interlayer developed in this work exhibits exceptional thermal stability compared to previously reported barrier materials[28,31-33,35,36]. Notably, the parabolic rate constant for the Mo-MPEA/P-SKD interface is measured at approximately 0.028 μΩ·cm^2·h$^{-1/2}$, a value that is comparable to the current state-of-the-art interlayer materials. Since a lower growth rate directly correlates with more stable electrical connection performance during long-term service, this minimal increment highlights the effective suppression of interfacial interdiffusion.

The mechanical response in Figure 5(f) shows a slight de-

crease in shear strength from about 18 MPa to approximately 16 MPa after 600 h aging. This limited reduction indicates that the joint retains most of its bonding strength despite the formation and growth of the reaction layer. This mechanical stability is attributed to the well-matched CTE between the Mo-MPEA and P-SKD, which fundamentally mitigates the generation of thermal mismatch-induced residual interfacial stresses, coupled with the sluggish growth of the interfacial reaction layer which prevents excessive brittle phase accumulation.

It should be noted that the electrical and mechanical properties reported in this work were evaluated based on the Mo-MPEA/P-SKD joint, whereas the Cu-W/Fe/Mo-MPEA region of the complete thermoelectric joint was not separately characterized. Since interfaces between metallic conductors generally form ohmic contacts, the incorporation of the Fe interlayer is not expected to make a significant contribution to the overall electrical resistance of the joint. Furthermore, shear testing demonstrated that fracture consistently occurred within the primary reaction layer of the Mo-MPEA/P-SKD joint rather than along the Fe-containing interfaces, suggesting that the Fe layer does not represent a mechanically critical weak point. Therefore, the Fe interlayer is expected to have a negligible influence on the overall electrical and mechanical performance of the thermoelectric joint.

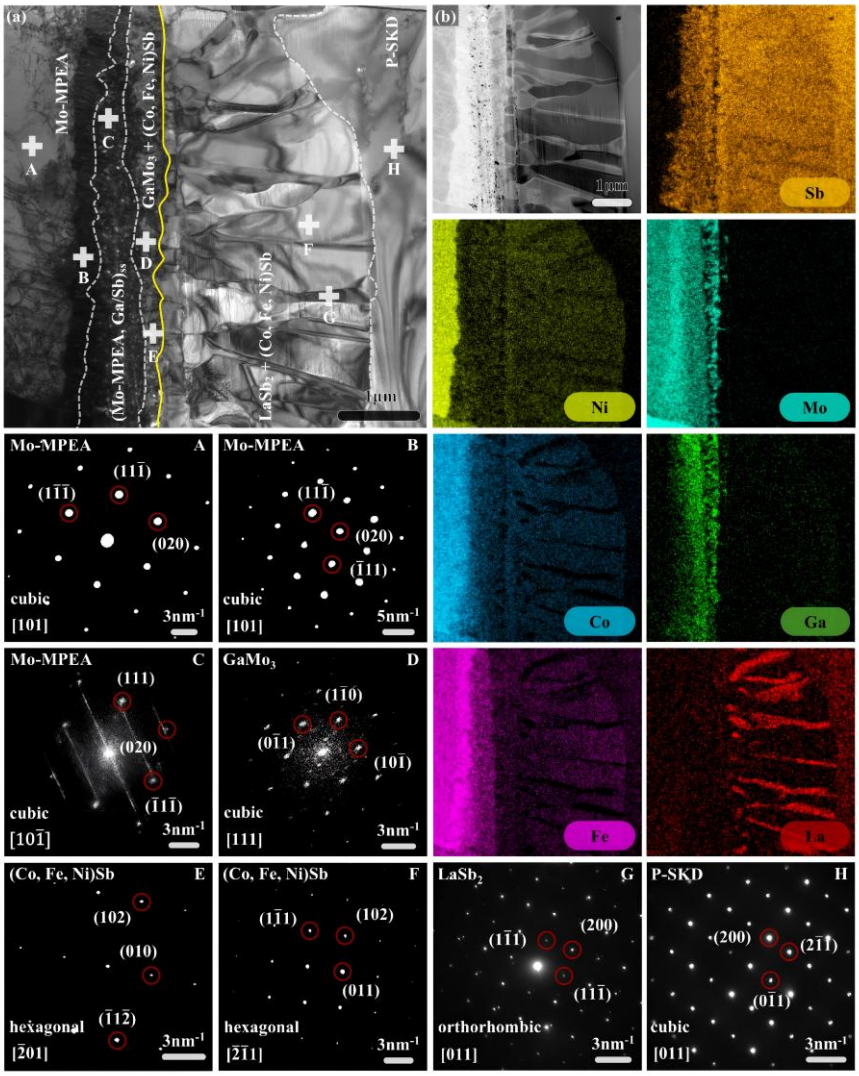

Figure 4. Interfacial reaction and metallurgical bonding mechanism of the Mo-MPEA/P-SKD interface. (a) Bright-field transmission electron microscopy (TEM) image of the initial Mo-MPEA/P-SKD interface and corresponding selected-area electron diffraction (SAED) patterns taken from different reaction regions, identifying Mo-MPEA, $GaMo_3$, (Co, Fe, Ni)Sb, $LaSb_2$, and P-SKD phases. The yellow solid line marks the initial contact interface. (b) High-angle annular dark-field (HAADF)- scanning transmission electron microscopy (STEM) image and STEM-energy dispersive X-ray spectroscopy (EDS) elemental maps of the interfacial region, revealing the elemental interdiffusion behavior

While the isothermal aging confirms the excellent diffusion barrier capability of the Mo-MPEA interlayer, practical thermoelectric modules inherently face complex environments involving steep temperature gradients and dynamic thermal cycling (e.g., repeated start-stop cycles in waste-heat recovery). Further evaluations under service-relevant thermomechanical conditions are valuable to comprehensively assess long-term interfacial durability. Furthermore, although the contact resistivity was measured at 300 K in this work, this value mainly reflects the quality of the initial electrical joint. According to the previous study[21], the total contact resistivity consists of the contributions from the interfacial reaction layer, diffusion layer, and contact resistance. Since the electrical resistivity of the formed (Co, Fe, Ni)Sb reaction products exhibits only weak temperature dependence[48] and the contact resistance is mainly determined by the interfacial microstructure, the overall contact resistivity is expected to remain relatively stable over the service temperature range.

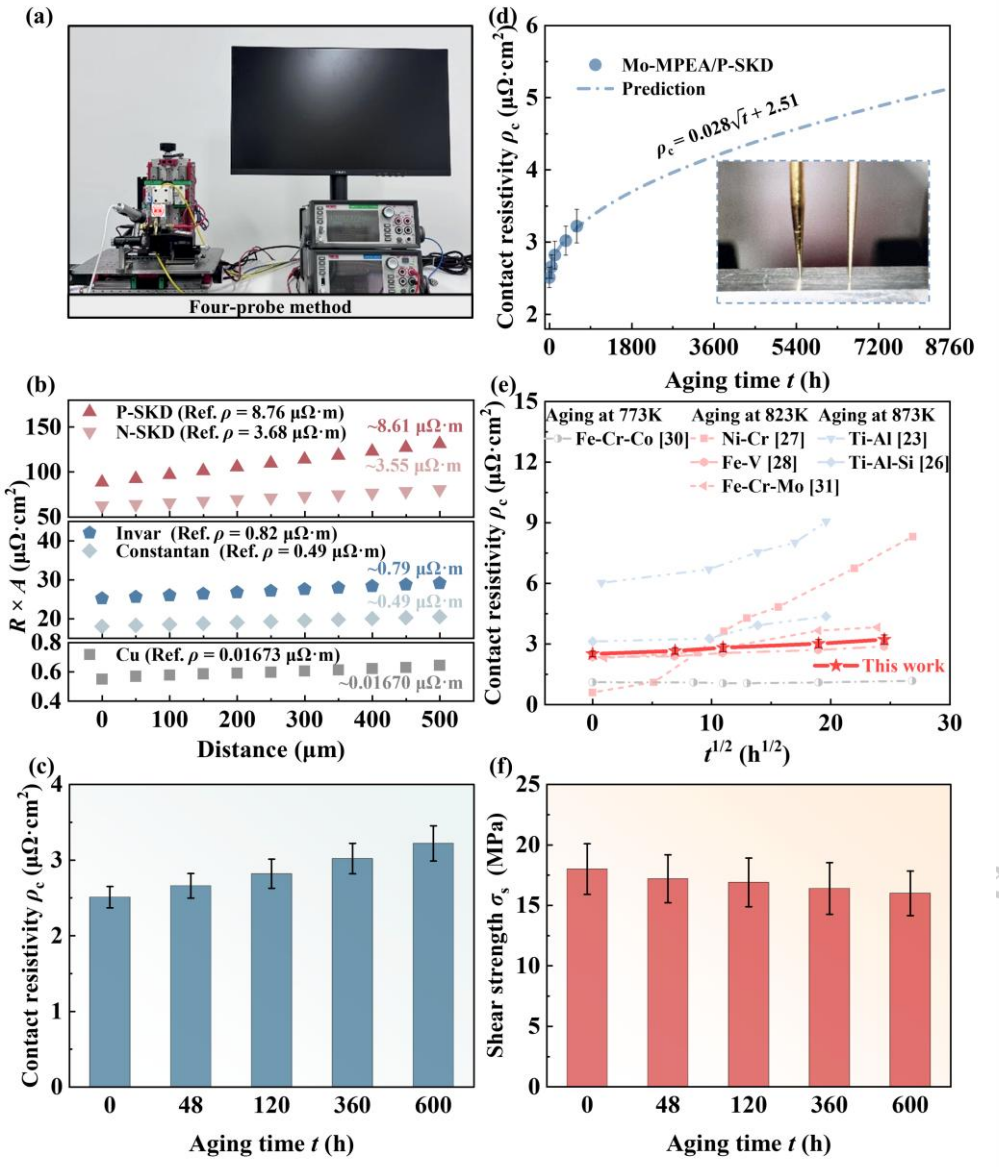

Figure 5. Electrical and mechanical stability of the Mo-MPEA/P-SKD interface throughout thermal aging at 823 K. (a) The microprobe-based electrical testing system. (b) Calibration of the contact-resistivity measurement using reference materials. (c) Contact resistivity of the Mo-MPEA/P-SKD joint as a function of aging time. (d) Correlation between contact resistivity and aging time, showing a $t^{1/2}$-dependent evolution consistent with diffusion-controlled reaction-layer growth. (e) The evolution of contact resistivity (ρ_c) as a function of the square root of aging time ($t^{1/2}$). Results of the Mo-MPEA/P-SKD joint are compared with various previously reported barrier materials aged at 773 K, 823 K, and 873 K. (f) Shear strength of the Mo-MPEA/P-SKD joint after different aging times.

Table 2. Comparison of shear strength σ_s, contact resistivity ρ_c and parabolic rate constant with different interlayers measured at 300 K.

Interlayers	σ_s (MPa)	ρ_c (μΩ·cm^2)	Parabolic rate constant (μΩ·cm^2·h$^{-1/2}$)	Aging temperature (K)
Fe-Cr-Co [30]	31	1.11	0.008	773
Ni-Cr [27]	13	0.9	0.30	823
Fe-V [28]	33	2.35	0.025	823
Fe-Cr-Mo [31]	17	2.31	0.073	823
Ti-Al [23]	26	1.04	0.11	873
Ti-Al-Si [26]	20	3.16	0.065	873
This work	18	2.51	0.028	823

4 Conclusions

In this work, a Mo-alloyed CoFeNi-based dual-phase multi-principal element alloy interlayer ($CoFeNiMo_{0.75}$) was engineered for the p-type skutterudite thermoelectric interface, and the interfacial reaction mechanism and evolution behavior were systematically investigated. The interdiffusion of multiple elements drives the decomposition of skutterudites, leading to interfacial reaction layer growth governed by diffusion-controlled kinetics. Adequate Mo alloying plays a critical role in establishing a multiple diffusion barrier effect without sacrificing thermal expansion compatibility: (i) Mo dissolved in the FCC matrix intensifies lattice distortion, thereby hindering elemental diffusion; (ii) the precipitated Mo-rich topologically close-packed μ phases exhibit extremely weak reactivity with skutterudites; and (iii) the dendritic μ phases distributed throughout the matrix increase the effective diffusion-path tortuosity. Owing to this dual-phase synergistic effect, the $CoFeNiMo_{0.75}/La_{0.8}Ti_{0.1}Ga_{0.1}Fe_{3.3}Co_{0.7}Sb_{12}$ interface exhibits excellent thermal stability. After aging at 823 K for 600 h, the reaction layer grew from ~4.2 μm to ~26.1 μm and the interfacial contact resistivity increased from ~2.51 μΩ·cm^2 to ~3.22 μΩ·cm^2, following parabolic kinetics well described by the Deal-Grove model. An ultralow parabolic rate constant of approximately 0.028 μΩ·cm^2·h$^{-1/2}$ was achieved, while the shear strength remained largely stable, decreasing only from 18 MPa to 16 MPa as a consequence of the matched thermal expansion and the slow interfacial reaction kinetics. This work not only demonstrates a viable multiple diffusion barrier strategy for decomposition-prone p-type skutterudites, but also provides a new design principle based on the dual-phase synergistic effect for controlling elemental diffusion in broader thermoelectric interfaces.

References

1 Zhao Wenyu,Liu Zhiyuan,Sun Zhigang *et al*.*Nature*[J],2017,549(7671):247-251

2 Heremans J P,Jovovic V,Toberer E S *et al*.*Science*[J],2008,321(5888):554-557

3 Xie Yu,Wu Shijun,Yang Canjun.*Applied Energy*[J],2016,164:620-627

4 He Jian,Tritt T.M.*Science*[J],2017,357(6358):eaak9997

5 Xie Liangjun,Yin Li,Yu Yuan *et al*.*Science*[J],2023,382(6673):921-928

6 Fu Yuntian,Ai Xin,Hu Zhongliang *et al*.*Nature Communications*[J],2024,15(1):9355

7 Zhang Qihao,Liao Jincheng,Tang Yunshan *et al*.*Energy and Environmental Science*[J],2017,10(4):956-963

8 Liu Weishu,Bai Shengqiang.*Journal of Materiomics*[J].2019,5(3):321-336

9 Le Wenkai,Yang Wenwei,Sheng Wenwen *et al*.*ACS Applied Materials and Interfaces*[J],2023,15(10):12611-12621

10 Liu Zhiyuan,Zhu Jianglong,Tong Xin *et al*.*Journal of Advanced Ceramics*[J],2020,9(6):647-673

11 Rogl G,Rogl P.*Current Opinion in Green and Sustainable Chemistry*[J],2017,4:50-57

12 Freer R,Ekren D,Ghosh T *et al*.*Journal of Physics:Energy*[J],2022,4(2):022002

13 Liu Ruiheng,Qiu Pengfei,Chen Xihong *et al*.*Journal of Materials Research*[J],2011,26:1813-1819

14 Chen Yuqi,Kawamura Y,Hayashi J *et al*.*Japanese Journal of Applied Physics*[J],2016,55(4):04EJ02

15 Li Xiaofang,Yao Honghao,Ma Baopeng *et al*.*Chemical Engineering Journal*[J],2025,525:170338

16 Zelenka F,Broz P,Vrestal J *et al*.*RSC Advances*[J],2019,9(37):21451-21459

17 Katarzyna P,Richard S T,Milena S *et al*.*Materials*,2018,11(12):2483

18 Gu Ming,Xia Xugui,Huang Xiangyang *et al*.*Journal of Alloys and Compounds*[J],2016,671:238-244

19 Zhang Qihao,Liao Jincheng,Tang Yunshan *et al*.Journal of Inorganic Materials[J],2018,33(8):889-894

20 Shao Xiao,Liu Ruiheng,Wang Liang *et al*.Journal of Inorganic Materials[J],2020,35(2):224-230

21 Chu Jing,Huang Jian,Liu Ruiheng *et al*.Nature Communications[J],2020,11:2723

22 Zhao Degang,Li Xiaoya,He Lin *et al*.Intermetallics[J],2009,17(3):136-141

23 Gu Ming,Xia Xugui,Li Xiaoya *et al*.Journal of Alloys and Compounds[J],2014,610:665-670

24 Zhang Qihao,Liao Jincheng,Tang Yunshan *et al*.Energy and Environmental Science[J],2017,10:956-963

25 Wan Shun,Song Qingfeng,Chen Hongyi *et al*.Cell Reports Physical Science[J],2023,4:101651

26 Li Junqin,Zhao Shiyuan,Chen Jiali *et al*.ACS Applied Materials and Interfaces[J],2020,12:44858-44865

27 Guo Fengkai,Shi Wenjing,Sun Yuxin *et al*.Acta Materialia[J],2025,284:120591

28 Pan Hui,Zhang Lixia, Geng Huiyuan *et al*.Materials Today Physics[J],2025,50:101635

29 Zhang Lixia,Pan Hui,Sun Zhan *et al*.ACS Applied Materials & Interfaces[J],2023,15(51):59912-59919

30 Shi Wenjing,Qin Dandan,Sun Yuxin *et al*.Advanced Energy Materials[J],2024,14(12):2303698

31 Pan Hui,Sun Zhan,Geng Huiyuan *et al*.Journal of Materiomics[J],2025,11(2):100859

32 Miracle D B,Senkov O N.Acta Materialia[J],2017,122:448-511

33 Zhang Jialun,Zhang Fandong,Chen Jian *et al*.Journal of Alloys and Compounds[J],2026,1051:186005

34 Krishna S A,Noble N,Radhika N *et al*.Journal of Manufacturing Processes[J],2024,109:583-606

35 Hsu W L,Tsai C W,Yeh A C *et al*.Nature Reviews Chemistry[J],2024,8(6):471-485

36 Verma V,Belcher C H,Apelian D *et al*,Progress in Materials Science[J],2024,142:101245

37 Li Jie,Wu Kaidi,Niu Lichong *et al*.Rare Metal Materials and Engineering[J],2023,52(12):4251-4259(in Chinese)

38 Zheng Fanlin,Sun Tianming,Chi Hanjuan *et al*.Rare Metal Materials and Engineering[J],2022,51(11):4039-4050 (in Chinese)

39 Li Zhiming,Pradeep K G,Deng Yun *et al*.Nature[J],2016,534:227-230

40 Wang Qiannan,Lu Yiping,Yu Qian *et al*.Scientific Reports[J],2018,8:14910

41 Singh P,Johnson D D,Tiarks J *et al*.Acta Materialia[J],2024,272(15):119952

42 Karch C.Modeling and Numerical Simulation of Material Science[J],2014,4(3):104-114

43 Peng Zhen,Guo Qingyu,Sun Jian *et al*.Rare Metal Materials and Engineering[J],2024,53(1):17-22 (in Chinese)

44 Zhang Yong,Zuo Ting Ting,Tang Zhi *et al*.Progress in Materials Science[J],2014,61:1-93

45 Lide D.R., CRC handbook of chemistry and physics (84th ed.), CRC Press, 2004

46 Chung D H,Liu X D,Yang Y.Journal of Alloys and Compounds[J],2020,846:156189

47 Liu W H,Lu Z P,He J Y *et al*.Acta Materialia[J],2016,116:332-342

48 Ahmed A,Han S.Journal of Alloys and Compounds[J],2016,686:540-548

多重扩散阻挡效应的双相多主元合金中间层用于 p 型方钴矿热电材料电界面

张凡董[1†]， 刘滨豪[1†]， 黄婧雯[1]， 邱聪[1]， 陈建[1]， 张嘉伦[1, 2, *]

（1. 功率半导体与集成技术全国重点实验室，先进半导体技术与应用教育部工程研究中心，半导体学院（集成电路学院），湖南大学，长沙 410082，中国）

（2. 长沙半导体技术与应用创新研究院，长沙 410082，中国）

摘 要：p型方钴矿及其电连接界面较差的热稳定性，严重制约了方钴矿基热电器件的可靠性。本文设计并制备了一种双相多主元合金中间层（$CoFeNiMo_{0.75}$），通过Mo合金化，在保持热膨胀匹配的同时，构筑了多重扩散阻挡效应。固溶于面心立方（FCC）基体中的Mo加剧了晶格畸变，从而有效抑制了元素的扩散。而弥散分布的枝晶状富Mo的析出相（μ相）则表现出较低的反应活性，并显著增加了有效扩散路径的曲折度。得益于这种双相协同机制，$CoFeNiMo_{0.75}/La_{0.8}Ti_{0.1}Ga_{0.1}Fe_{3.3}Co_{0.7}Sb_{12}$ 界面表现出优异的热稳定性。在823 K下600 h

热老化实验后，界面接触电阻率从仅约2.51 μΩ·cm^{2}增加至3.22 μΩ·cm^2，其演变遵循抛物线动力学规律，且具有极低速率常数（约为0.028 μΩ·cm^2·h$^{-1/2}$）。同时，界面剪切强度基本保持稳定（约16 MPa）。上述结果表明，双相策略在为下一代热电界面构建稳固、多层级的扩散阻挡层方面具有巨大潜力。

关键词: p型方钴矿；多主元合金；双相结构；扩散阻挡层；热电界面

作者简介：张凡董，男，1999 年生，湖南大学半导体学院（集成电路学院），湖南 长沙 410082，E-mail:zhangfandong@hnu.edu.cn

刘滨豪，男，2004 年生，湖南大学半导体学院（集成电路学院），湖南 长沙 410082，E-mail:13898550062@163.com